

Can cosmic rays explain the high ionisation rates in the Galactic Centre?

S. Ravikularaman¹, S. Recchia², V. H. M. Phan³ and S. Gabici¹

¹ Université Paris Cité, CNRS, Astroparticule et Cosmologie, F-75013 Paris, France
e-mail: ravikularaman@apc.in2p3.fr

² INAF-Osservatorio Astronomico di Brera, Via Bianchi 46, I-23807 Merate, Italy

³ Sorbonne Université, Observatoire de Paris, PSL Research University, LERMA, CNRS UMR 8112, 75005 Paris, France

June 24, 2024

ABSTRACT

Context. The H₂ ionisation rate in the Central Molecular Zone, located in the Galactic Centre region, is estimated to be $\zeta \sim 2 \times 10^{-14} \text{ s}^{-1}$, based on observations of H₃⁺ lines. This value is 2-3 orders of magnitude larger than that measured anywhere else in the Galaxy.

Aims. Due to the high density of the gas in the Central Molecular Zone, UV and X-ray photons do not penetrate this region. Hence, cosmic rays are expected to be the exclusive agents of ionisation. A high cosmic-ray density has been invoked to explain the unusually high ionisation rate. However, this excess is not seen in the γ -ray emission from this region, which is produced by high-energy cosmic rays. Therefore, an excess is expected only in the low-energy cosmic-ray spectrum. Here, we derive constraints on this hypothetical low-energy component in the cosmic-ray spectra and we question its plausibility.

Methods. To do so, we solve numerically the cosmic-ray transport equation in the Central Molecular Zone, considering spatial diffusion, advection in the Galactic wind, reacceleration in the ambient turbulence, and energy losses due to interactions with matter and radiation in the interstellar medium. We derive stationary solutions under the assumption that cosmic rays are continuously injected by a source located in the Galactic Centre. The high-energy component in the cosmic-ray spectrum is then fitted to available γ -ray and radio data, and a steep low-energy component is added to the cosmic-ray spectrum to explain the large ionisation rates.

Results. We find that injection spectra of p^{-7} for protons below $p_{\text{enh},p}c \simeq 780 \text{ MeV}$ and $p^{-5.2}$ for electrons below $p_{\text{enh},e}c = 1.5 \text{ GeV}$ are needed to reach the observed ionisation rates. This corresponds to an extremely large cosmic-ray power of the order $\sim 10^{40-41} \text{ erg s}^{-1}$ injected at the Galactic Centre.

Conclusions. We conclude that cosmic rays alone can not explain the high ionisation rates in the Galactic Centre region.

Key words. Galaxy: center – ISM: cosmic rays – Gamma rays: ISM – Radio continuum: ISM – Radiation mechanisms: non-thermal – ISM: clouds

1. Introduction

At the centre of the Milky Way, located at $\sim 8.5 \text{ kpc}$ from the Solar system, lies the supermassive black hole Sagittarius A* (Sgr A*). It is surrounded by the Galaxy's densest and most massive molecular clouds (MCs), forming an asymmetric ring-like structure of molecular Hydrogen gas (Ferrière et al. 2007). This region is named the Central Molecular Zone (CMZ) and occupies a roughly cylindrical volume of radius of $\approx 200 \text{ pc}$ and height $\approx 100 \text{ pc}$.

The star formation rate in the CMZ is $\approx 0.07^{+0.08}_{-0.02} M_{\odot} \text{ yr}^{-1}$, a number significantly lower than expected given the amount of dense gas in this region (Henshaw et al. 2023). Hence, it is vital to understand the process and requirements for star formation in this region. One of the critical ingredients for star formation is the gas ionisation rate, which measures the number of ionisations an atom or a molecule of hydrogen undergoes per unit of time. A few different definitions exist for this quantity (Neufeld & Wolfire 2017). In this paper, we refer to the ionisation rate as the production rate of H₂⁺ ions per hydrogen molecule.

The ionisation potential of H₂ is $I = 15.426 \text{ eV}$. Both cosmic rays (CRs) and photons (UV, X-rays) can ionise H₂:



but it is believed that the first reaction largely dominates over the second one in MCs, as ionising photons cannot penetrate large column densities of gas (McKee 1989). Among CRs, those with particle energy in the sub-GeV domain are believed to be most effective in ionising interstellar matter (see e.g. Gabici 2022, and references therein).

The ionisation of molecular hydrogen is followed by the extremely rapid ion-neutral reaction (Oka 2006):



leading to the production of H₃⁺ ions. Note that other ionisation processes, such as double or dissociative ionisation, are negligible compared to these processes (Padovani et al. 2009) and will be ignored in the following.

H₃⁺ is destroyed through dissociative recombination, according to one of the two following reactions (Oka 2006):



The rate of H_3^+ destruction through recombination per unit volume is:

$$r_{des}^{\text{H}_3^+} = k_e n(\text{H}_3^+) n(e^-) \quad (6)$$

where k_e is the Langevin rate constant for this reaction determined in laboratory experiments (McCall et al. 2003). For typical cloud temperatures of few 10s of degrees, $k_e \approx 10^{-7} \text{ cm}^3 \text{ s}^{-1}$. By balancing the rates of formation and destruction of H_3^+ , we obtain an expression for the ionisation rate:

$$\zeta_{CR}^{\text{H}_2} = \frac{2k_e x_e N(\text{H}_3^+)}{f_{\text{H}_2} L} \quad (7)$$

where x_e is the electron fraction, $f_{\text{H}_2} = 2n(\text{H}_2)/n_{\text{H}}$ is the fraction of molecular hydrogen, $N(\text{H}_3^+)$ is the H_3^+ column density along the line of sight of length L . The latter quantity is the most uncertain and is usually estimated by assuming that clouds are roughly spherical. The other quantities on the right side of the equation can be constrained from observations (see e.g. McCall et al. 2003, and references therein for the case of a diffuse cloud towards ζ Persei).

Observations towards various lines of sight in the Galaxy have shown that the ionisation rate is of the order of $\approx 10^{-16} \text{ s}^{-1}$ in diffuse clouds and $\approx 10^{-17} \text{ s}^{-1}$ in dense clouds, with a quite large dispersion around these values (Caselli et al. 1998; Indriolo & McCall 2012; Padovani et al. 2009; Phan et al. 2018). These values are much larger (a factor of 10 to 100) than expected if one makes the assumption that the CR intensity changes only very mildly across the Galaxy (Phan et al. 2018). A possible solution to this puzzle is to assume that, in fact, the intensity of low-energy (ionising) CRs varies spatially, and it is larger close to CR accelerators (Phan et al. 2021, 2023).

The discrepancy is even more striking in the region very close to the Galactic Centre (GC). By analysing the absorption spectra of various stars, Oka et al. (2005) measured the H_3^+ column density and concluded that the ionisation rate in the CMZ is $(2-7) \times 10^{-15} \text{ s}^{-1}$. Based on new sightlines from Geballe & Oka (2010), Goto et al. (2011) concluded that the ionisation rates in the CMZ were $> 10^{-15} \text{ s}^{-1}$, later corroborated by other infrared observations (Goto et al. 2014). Le Petit et al. (2016) questioned the validity of the linear relation between $N(\text{H}_3^+)$ and ζ and suggested it only holds up to a certain value of the ionisation rate. Using the Meudon PDR code (Le Petit et al. 2006), they found that the ionisation rate in the GC must be $1-11 \times 10^{-14} \text{ s}^{-1}$. This value is in accordance with Oka et al. (2019)'s most recent analysis of 30 stellar spectra, where they raised their initial estimate by an order of magnitude to $\zeta_{\text{CMZ}} = 2 \times 10^{-14} \text{ s}^{-1}$.

Yusef-Zadeh et al. (2007) used another method to constrain the ionisation rate. They analysed γ -rays, radio synchrotron emissions and the Iron $K\alpha$ line and concluded that along certain lines of sight, the ionisation rate could be as high as $5 \times 10^{-13} \text{ s}^{-1}$. Later they reduced this upper limit to 10^{-14} s^{-1} (Yusef-Zadeh et al. 2013).

Molecules like H_3O^+ are produced in MCs as the result of chemical reaction chains initiated by the ionisation of molecular hydrogen. These molecules have also been used to constrain the ionisation rate in the vicinity of the GC. In particular, van der Tak et al. (2006) analysed H_3O^+ maps of the Sgr B2 region and found that an ionisation rate of $4 \times 10^{-16} \text{ s}^{-1}$ reproduced the $\text{H}_3\text{O}^+/\text{H}_2\text{O}$

ratio in the cloud envelope. Although this value is lower than early estimates, a more recent Herschel survey of H_3O^+ suggests higher ionisation rates of $> 10^{-15} \text{ s}^{-1}$ (Indriolo et al. 2015).

Most recently, the observations of other molecules have also hinted towards a high ionisation rate. Ginsburg et al. (2016) observed $J=3-2$ transition of para-formaldehyde ($p\text{-H}_2\text{CO}$) to estimate the gas temperature of the CMZ and set the upper limit for the ionisation rate as 10^{-14} s^{-1} . The measured abundance of PO^+ (Rivilla et al. 2022) and HCOS^+ (Sanz-Novo et al. 2024) towards the G+0.693-0.027 MC in the CMZ also imply an ionisation rate of $10^{-15} - 10^{-14} \text{ s}^{-1}$.

The values of the ionisation rate measured in the CMZ employing various techniques range then from $\approx 10^{-15}$ to $\approx 10^{-13} \text{ s}^{-1}$, which are much larger (up to few orders of magnitude!) than the values measured from diffuse and dense clouds in the Galaxy. Although an increase in the CR density, and therefore in the CR ionisation rate, might be expected towards the centre of the Galaxy, the increase is predicted to be at most of a factor of a few (see e.g. Wolfire et al. 2003). It follows that, in order to explain the extremely large ionisation rates seen in the CMZ, one should invoke an equally large excess in sub-GeV CRs there, and that this excess is due to a *new* component in the CR spectrum, unrelated to the CR background that pervades the entire Galaxy.

This is even more puzzling, as tracers of the spatial distribution of higher-energy (GeV) CRs in the Galaxy, such as γ -rays produced in CR interactions with interstellar matter, do not reveal the presence of a significant excess in the CMZ (see e.g. Fig. 9 in Gabici 2022, and references therein). This implies that a large excess must only be present in low-energy CRs.

Remarkably, the H.E.S.S. Collaboration reported on the detection of the CMZ in TeV γ -rays. The spatial morphology of the emission indicates that a source of CRs has to be present in the vicinity of Sgr A* and that such a source is most probably a continuous injector of CRs (HESS Collaboration et al. 2016). The excess in multi-TeV CRs derived from such measurements is of a factor of several, and indicates that a new component in the spectrum of high-energy CRs is indeed present in the CMZ.

In this paper, we study whether it is possible for CRs to cause the very large ionisation rates observed in the CMZ. In particular, we will assume that a CR accelerator is present in the vicinity of the GC and that such an accelerator injects particles continuously into the CMZ. Our goal is to constrain the spectral energy distribution and the rate at which CRs have to be injected in order to explain the measured ionisation rates. We conclude that the power requirement to fit data is exceedingly large, and therefore, the cause of the large ionisation rate has to be searched elsewhere.

In the next section, we describe the model for CR transport in the CMZ, including all the fiducial parameters. In Sec.3 and 4 we constrain the high-energy CR proton and electron spectra from diffuse γ -ray and radio observations of the CMZ, respectively. We extrapolate these high-energy spectra to lower energies and compute the ionisation rates in Sec.5. As these values are smaller by several orders of magnitude than the measured ionisation rates in the CMZ, we add a steep power-law component in the injection spectrum of CRs, and we try steeper and steeper slopes until the predicted ionisation rates reach the observed values. After studying the spatial variation of this value across the entire CMZ, we discuss the uncertainty introduced by the unknown depth L into the CMZ of the stars used for H_3^+ absorption measurements. Most importantly, we compute the power W_{CR} of CRs and their energy density n_{CR} needed to explain the measurements of the ionisation rate. We show in Sec.6

that the CR spectra suitable to reproduce the large ionisation rates contradict other observations of the CMZ, and we eventually conclude that CRs can not explain the large ionisation rates (Sec.7).

2. Cosmic-ray transport in the CMZ

The CMZ is modelled as a cylinder of uniform gas density n_{CMZ} . The cylinder has a radius $R_{CMZ} \sim 200$ pc (Ferrière et al. 2007), and height $H_{CMZ} \sim 100$ pc, and is centred around Sgr A* located at $D_{GC} \sim 8.5$ kpc (see Fig. 1). The gas mass of the CMZ has been estimated to be $M_{CMZ} \sim 6 \times 10^7 M_{\odot}$ (Dahmen et al. 1998; Tsuboi et al. 1999), which implies that the average gas density is $n_{CMZ} = 1.5 \times 10^2 \text{ cm}^{-3}$. The CMZ is embedded in the Galaxy's gaseous disk, assumed to have the same height of the CMZ, H_{CMZ} , and characterised by a gas density $n_{disk} \sim 1 \text{ cm}^{-3}$. Outside of the Galactic disk, the gas density is set equal to $n_{out} \sim 10^{-2} \text{ cm}^{-3}$, which is appropriate to describe the Galactic halo.

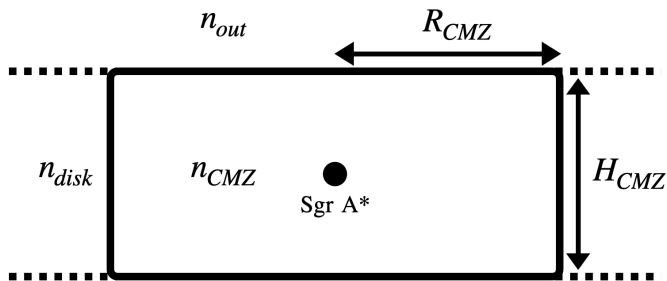


Fig. 1: Schematic edge-on view of the CMZ modelled as a cylinder of radius $R_{CMZ} = 200$ pc and height $H_{CMZ} = 100$ pc centred around Sgr A*. The average density inside the CMZ is $n_{CMZ} = 1.5 \times 10^2 \text{ cm}^{-3}$. The density in the Galactic disk and halo are taken as $n_{disk} \sim 1 \text{ cm}^{-3}$ and $n_{out} \sim 10^{-2} \text{ cm}^{-3}$.

The CMZ has been detected in very high energy γ rays by the HESS Collaboration (Aharonian et al. 2006). The spatial correlation between the observed γ rays and the gas distribution in the region suggests that such emission is due to the decay of neutral pions produced in inelastic interactions between CRs and ambient gas. Moreover, a study of the morphology of the γ -ray emission suggests that the CRs responsible for such emission have been produced in the past by an accelerator located very close to the GC and that such an accelerator continuously injects relativistic particles in the surrounding medium (HESS Collaboration et al. 2016).

After the escape from the accelerator, the transport of relativistic particles in and around the CMZ is dictated by spatial diffusion in the turbulent ambient magnetic field and advection in the Galactic wind. At the same time, particles suffer energy losses due to interactions with ambient matter and radiation and are reaccelerated due to scattering off ambient MHD waves.

In order to describe the transport of CRs in the CMZ region, it is convenient to adopt a cylindrical set of coordinates centred on the GC, with the radial coordinate r directed along the Galactic plane and the height z orthogonal to it. The equation describing the evolution in time, space, and momentum of the CR particle distribution function $f(t, r, z, p)$ is :

Table 1: Physical parameters adopted to model the CMZ. See the text for the definitions of each parameter.

Parameter	Value
D_{GC}	8.5 kpc
R_{CMZ}	2.0×10^2 pc
H_{CMZ}	1.0×10^2 pc
V_{CMZ}	$3.4 \times 10^{62} \text{ cm}^3$
M_{CMZ}	$6 \times 10^7 M_{\odot}$
n_{CMZ}	$1.5 \times 10^2 \text{ cm}^{-3}$
n_{disk}	1.0 cm^{-3}
n_{out}	$1.0 \times 10^{-2} \text{ cm}^{-3}$
$D(10 \text{ TeV})$	$6 \times 10^{29} \text{ cm}^2 \text{ s}^{-1}$
β	0.3
B_{CMZ}	$1.5 \times 10^2 \mu\text{G}$
B_{disk}	$3.0 \mu\text{G}$
B_{out}	$3.0 \mu\text{G}$
v_A	$1.0 \times 10^2 \text{ km s}^{-1}$
v_w	$2.0 \times 10^2 \text{ km s}^{-1}$
$T_{NIR} (\kappa_{NIR})$	0.3 eV (1.3×10^{-11})
$T_{FIR} (\kappa_{FIR})$	6×10^{-3} eV (9×10^{-6})
$T_{CMB} (\kappa_{CMB})$	2.35×10^{-4} eV (0.99)

$$\begin{aligned} \frac{\partial f}{\partial t} = & D_{rr} \frac{\partial^2 f}{\partial r^2} + \left(\frac{D_{rr}}{r} + \frac{\partial D_{rr}}{\partial r} \right) \frac{\partial f}{\partial r} + D_{zz} \frac{\partial^2 f}{\partial z^2} + \frac{\partial D_{zz}}{\partial z} \frac{\partial f}{\partial z} - v_w \frac{\partial f}{\partial z} \\ & + \frac{1}{p^2} \frac{\partial}{\partial p} \left(p^2 D_{pp} \frac{\partial f}{\partial p} \right) + \frac{p}{3} \frac{\partial v_w}{\partial z} \frac{\partial f}{\partial p} - \frac{1}{p^2} \frac{\partial}{\partial p} (\dot{p} p^2 f) + Q \end{aligned} \quad (8)$$

where D_{rr} and D_{zz} are the CR spatial diffusion coefficients along r and z , respectively, v_w is the Galactic wind velocity (assumed to be directed along the z -axis), D_{pp} the CR diffusion coefficient in momentum (particle reacceleration), \dot{p} the momentum loss rate, and Q the particle injection rate. In the following, we will consider the case of an isotropic and spatially uniform diffusion ($D(p) = D_{rr} = D_{zz}$) and a wind speed independent of z .

The first four terms on the right-hand side of Eq.8 describe the spatial diffusion of particles, while the fifth term refers to advection in the Galactic wind. Diffusion in momentum space (reacceleration) is modelled by the sixth term, while the seventh represents adiabatic losses. Finally, the eighth term accounts for momentum losses at a rate \dot{p} due to particle interaction with ambient matter and radiation.

The CR spatial diffusion coefficient is difficult to constrain from observations. However, in order to have diffusive transport of CRs in the CMZ, the mean free path for spatial diffusion has to be much smaller than the size of the region, R_{CMZ} . This converts into an upper limit for the CR diffusion coefficient as $D \ll cR/3 \approx 6 \times 10^{30} \text{ cm}^2 \text{ s}^{-1}$. Following HESS Collaboration et al. (2016), we assume the diffusion to be isotropic and the diffusion coefficient is:

$$D_{rr} = D_{zz} = D(p) = 6 \times 10^{29} \left(\frac{pc}{10 \text{ TeV}} \right)^{\beta} \text{ cm}^2 \text{ s}^{-1} \quad (9)$$

with $\beta = 0.3$. Although theoretical considerations suggest that a break might appear in $D(p)$ in the low-energy (transrelativistic) regime (see e.g. Phan et al. 2021, and references therein), we adopt here a pure power-law scaling down to arbitrarily low

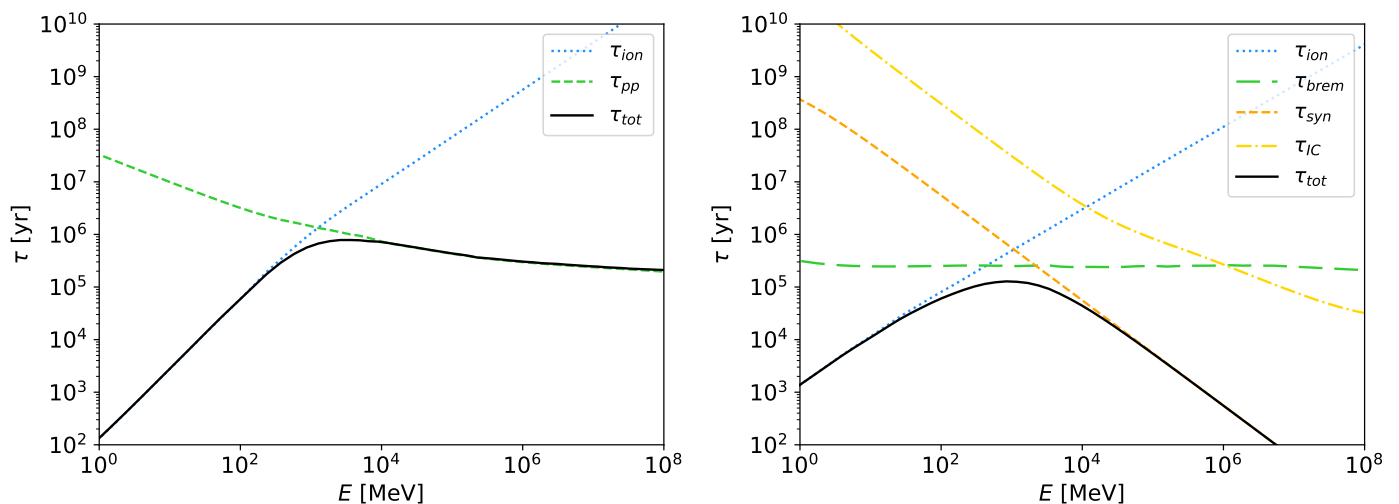


Fig. 2: Characteristic timescales for CR energy losses in the CMZ (see Table 1 to see what parameters were adopted). **Left:** Proton loss times for ionisation and p-p interactions. **Right:** Electron loss times for ionisation, synchrotron, Bremsstrahlung and inverse Compton scattering.

particle energies, as the presence of a break will not affect any of our results. Note that our choice of D makes the transport of CRs diffusive up to particle energies in the multi-PeV domain.

The advection of CRs is caused by a Galactic wind with a discontinuous velocity at $z = 0$ of the form $v(z) = \text{sgn}(z)v_w$. The value of the wind speed v_w in the CMZ region is uncertain, with estimates spanning the range going from 200 km s^{-1} to 1200 km s^{-1} (see e.g. Crocker et al. 2011). To maximise the impact of CRs in the region, we adopt here the value corresponding to the lower bound in that interval, i.e., $v_w \sim 200 \text{ km s}^{-1}$. Larger values of v_w would increase advection efficiency, resulting in lower densities of CRs in the CMZ region.

The CR momentum diffusion coefficient D_{pp} is expected to be inversely proportional to the spatial diffusion coefficient, as many repeated scatterings onto (moving) magnetic irregularities would enhance diffusion in momentum space while suppressing spatial diffusion. If magnetic perturbances are Alfvén waves, the following heuristic expression can be adopted (Thornbury & Drury 2014):

$$D_{pp}(p) = \frac{p^2 v_A^2}{9D(p)} \quad (10)$$

where v_A is the Alfvén velocity.

The momentum loss rate, \dot{p} , accounts for energy loss processes due to interactions of CRs with ambient matter and radiation (see Padovani et al. 2018; Gabici 2022, and references therein). It describes ionisation losses at low particle energies, while at larger energies, Bremsstrahlung, synchrotron and inverse Compton losses dominate for CR electrons and proton-proton inelastic interactions for CR protons.

Ionisation, pion production, and Bremsstrahlung losses depend only on the ambient gas density and are treated in the following as in Padovani et al. (2018). To describe inverse Compton losses, we follow Khangulyan et al. (2014) and consider a target photon field with three thermal (grey body) components: near-infrared (NIR), far-infrared (FIR) and the Cosmic Microwave Background (CMB), equal to those adopted by Hinton & Aharonian (2007) to model the radiation density in the CMZ region. For synchrotron losses, the value of the ambient magnetic field B is kept as a free parameter, but its value is constrained to be

larger than $50 \mu\text{G}$, a lower limit derived observationally for the CMZ by Crocker et al. (2010). The energy loss time for each mechanism l is then defined as:

$$\tau_l = E/\dot{E} \quad (11)$$

where E is the particle kinetic energy and $\dot{E} = dE/dt$ the energy loss rate. The loss times are shown in Fig. 2 for CR protons (left) and electrons (right).

Finally, the injection of CR particles is considered point-like in space and continuous in time. Particle spectra are assumed to be power laws (or broken power laws, as in Sec. 4.1) in momentum, giving:

$$Q_i(r, z, p) = Q_{p,i}(p) \frac{\delta(r)}{2\pi r} \delta(z) \quad (12)$$

where

$$Q_{p,i}(p) = Q_{0,i} \left(\frac{pc}{10 \text{ TeV}} \right)^{-\delta_i} \quad (13)$$

where the subscript i can refer to either protons ($i = p$) or electrons ($i = e$).

For each process affecting the propagation of CRs, it is possible to define a characteristic timescale based on the geometry of the CMZ and typical physical parameters that characterise that region (see Table 1). This gives us an idea of the relative importance of a mechanism at any given energy (see Fig. 3 where all relevant timescales are shown).

The timescale for spatial diffusion is defined as the time needed for a CR of momentum p to diffuse across a distance of R_{CMZ} :

$$\tau_{diff}(p) = \frac{R_{CMZ}^2}{6D(p)}. \quad (14)$$

The advection timescale is defined as the time needed for a particle to be advected over a vertical distance of $H_{CMZ}/2$:

$$\tau_{adv}(p) = \frac{H_{CMZ}}{2v_w}. \quad (15)$$

The timescale for reacceleration is defined as the time required for a particle to reach a momentum p :

$$\tau_{\text{reac}}(p) = \frac{p^2}{6D_{pp}(p)}. \quad (16)$$

Note that the ratio between the reacceleration and diffusion timescale is:

$$\frac{\tau_{\text{reac}}}{\tau_{\text{diff}}} = \frac{9D^2}{v_A^2 R_{\text{CMZ}}^2} \sim 1.6 \times 10^3 \left(\frac{D}{10^{28} \text{cm}^2/\text{s}} \right)^2 \left(\frac{v_A}{10 \text{km/s}} \right)^{-2} \quad (17)$$

which is large for any plausible value of the Alfvén speed and of the diffusion coefficient. Therefore, in the following, we fix $v_A = 100 \text{ km s}^{-1}$ as this parameter does not significantly affect our results. Finally, the loss timescale is calculated separately for protons and electrons using the loss times (Eq. 11) for all the mechanisms considered.

The steady-state solution for a given injection spectrum is obtained by solving the transport equation numerically with a Crank-Nicholson scheme (Evoli et al. 2017; Kissmann 2014; Press et al. 1992) where the delta-function in space describing particle injection (Eq. 12) is modelled as a narrow Gaussian.

The physical parameters adopted to compute all the characteristic times are given in Table. 1.

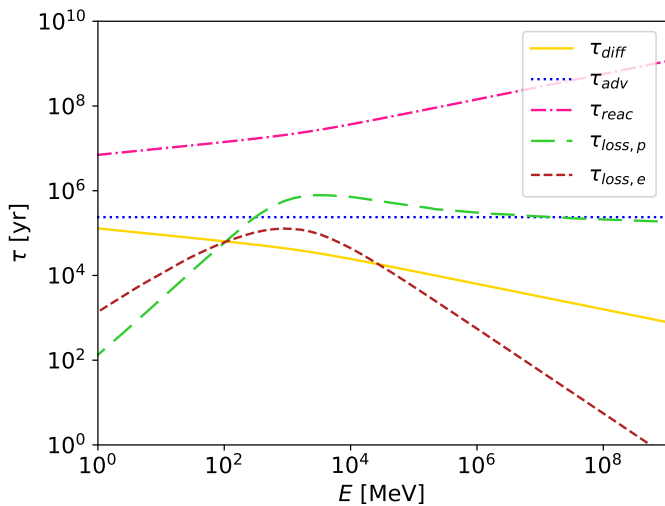


Fig. 3: Characteristic timescales for spatial diffusion, advection, reacceleration and losses for protons and electrons. The fiducial parameters are given in Table. 1.

3. γ -ray observations of the CMZ

The γ -ray emission from the CMZ has been observed by the High Energy Stereoscopic System (H.E.S.S.) (Aharonian et al. 2006; HESS Collaboration et al. 2016), the Fermi Gamma-ray Space Telescope (Gaggero et al. 2017), the Very Energetic Radiation Imaging Telescope Array System (VERITAS) (Adams et al. 2021) and the Major Atmospheric Gamma Imaging Cherenkov (MAGIC) Telescopes (MAGIC Collaboration et al. 2020). Combining the data from H.E.S.S. and Fermi, we consider GeV-TeV observations of the region within $|l| < 0.8^\circ$ and $|b| < 0.3^\circ$ called the Galactic Ridge (Aharonian et al. 2006; Gaggero et al. 2017) and an open annulus centred on Sgr A* with $\theta_{\text{inner}} = 0.15^\circ$ and $\theta_{\text{outer}} = 0.45^\circ$ known as the *pacman* region (HESS Collaboration et al. 2016).

The γ -rays observed from the Galactic disk result from the interactions of CRs with matter and radiation in the interstellar medium. The dominant process of γ -ray production is the interaction of CR protons with nuclei in the ISM. Leptonic processes such as inverse Compton scattering and non-thermal Bremsstrahlung might also contribute to the γ -ray emission (though they are expected to be subdominant in the CMZ).

The CMZ region is characterised by a very large gas density, and its γ -ray emission correlates quite well with the spatial distribution of interstellar matter, pointing quite unambiguously to a hadronic origin of the observed γ -rays (Aharonian et al. 2006). A more detailed analysis of the H.E.S.S. data suggests that the γ -ray emission is produced by CR nuclei that escaped from an accelerator located very close to the GC, which has been injecting particles in the surrounding medium for an extended period of time.

In the remaining of this Section, we will make use of the CR transport code described in Sec. 2, and we will estimate the γ -ray emission produced by CR nuclei and electrons which have been produced by such source and are now filling the CMZ.

In order to estimate the spectrum of γ -rays produced in hadronic proton-proton interactions, we will make use of the parameterisations of cross sections provided by Kafexhiu et al. (2014), including the nuclear enhancement factor that accounts for the presence of nuclei heavier than protons in both CRs and interstellar matter.

To model inverse Compton scattering, we consider interactions between relativistic electrons and soft photons present in the CMZ, following the approach presented in Khangulyan et al. (2014). The thermal components of the radiation field in the CMZ are near-infrared (NIR) peaking at a photon energy of 0.3 eV, far-infrared (FIR) at 6×10^{-3} eV and the Cosmic Microwave Background (CMB) at 2.35×10^{-4} eV (Hinton & Aharonian 2007). The respective energy densities are 9, 1 and 0.26 eV cm^{-3} . Each component is assumed to be characterised by a diluted black-body spectrum, with the dilution factor κ computed using the Stefan-Boltzmann law:

$$\kappa = \frac{wc}{4\sigma_{sb}T^4} \quad (18)$$

where w is the photon energy density, c the speed of light, σ_{sb} the Stefan-Boltzmann constant and T the photon temperature.

Finally, Bremsstrahlung radiation is produced when electrons decelerate in the Coulomb field of an ion. The emitted γ -ray radiation is modelled using the cross section appropriate for interactions of energetic electrons with neutral molecular hydrogen given in Schlickeiser (2002).

3.1. Derivation of cosmic-ray proton injection spectrum

In this section, we make use of the CR transport code described above to model the propagation of CRs that escaped the accelerator located in the GC and now fill the CMZ region. The time-dependent Eq. 8 is evolved in time until stationarity is reached. Then, the γ -ray emission from interactions of both CR nuclei and electrons in the ISM is computed. The spatial correlation between the γ -ray emission and the distribution of dense gas in the CMZ suggests a hadronic origin of the γ -ray photons (HESS Collaboration et al. 2016). So, the fit to available data allows us to derive the injection spectrum for CR protons. We will also consider and critically discuss leptonic scenarios where the γ -ray data will be used as an upper limit for the contribution from inverse Compton scattering and relativistic Bremsstrahlung.

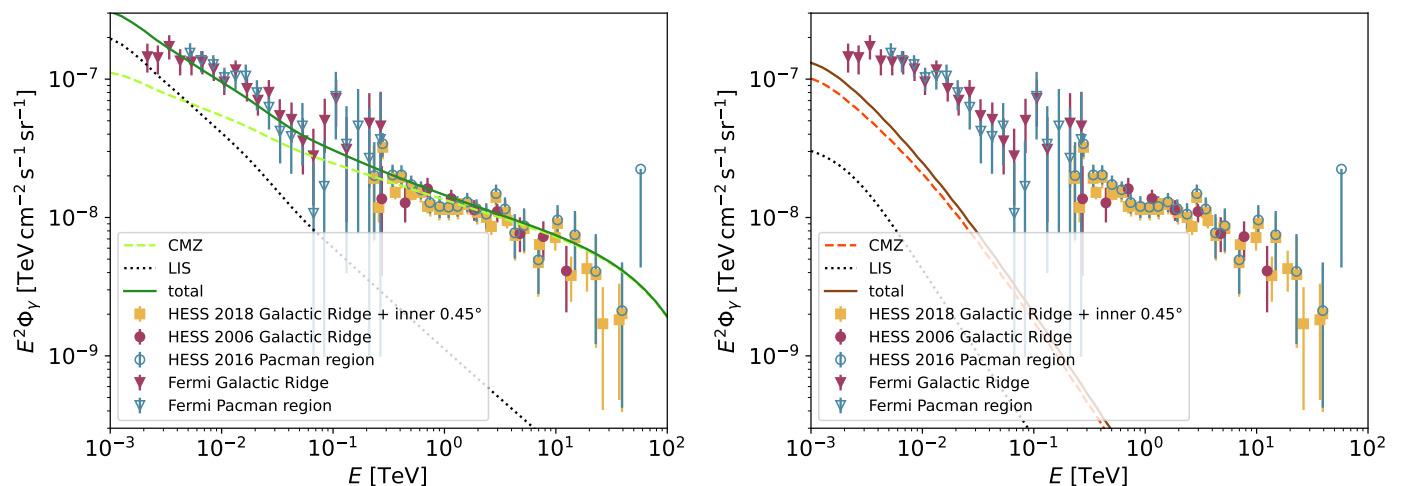


Fig. 4: γ -ray data for the CMZ region. Curves show theoretical results for hadronic (left panel) and leptonic (right panel) scenarios. Dashed lines show the emission from CRs accelerated within the CMZ (in a source located at the GC), while dotted lines show the contribution from ambient cosmic rays, assumed to have a spectrum equal to the local interstellar one (LIS).

The left and right panels of Fig. 4 show the observed γ -ray spectrum of the CMZ region, together with curves showing the results of our hadronic and leptonic models obtained by solving Eq. 8. Data points refer to Fermi and H.E.S.S. observations, as indicated in the figure inset.

The model curves shown in the figure refer to the emission from CR nuclei (left panel) and CR electrons (right panel). The long-dashed lines show our predictions for the γ -ray emission generated by CRs accelerated by the source located in the GC. Dotted lines show the emission coming from the interactions of background Galactic CRs that are known to fill the entire Galactic disk. As the spatial gradient of such latter component is believed to be very small, we assume that background CRs have the same intensity as those measured in the local interstellar medium (the label LIS stands for Local Interstellar Spectrum) by Voyager and AMS-02 (see e.g. Gabici 2022, and references therein). The γ -ray emission from background CR nuclei dominates the flux in the GeV energy domain, but it becomes subdominant in the TeV one. On the other hand, the emission from background CR electrons is always largely subdominant.

From Fig. 4 (left panel), it can be seen that the hadronic scenario provides a good fit to γ -ray data if the injection spectrum of CR protons is characterised by:

$$Q_{p,p}(10 \text{ TeV}) = 1.1 \times 10^{29} \text{ MeV}^{-1} \text{ s}^{-1} \quad (19)$$

$$\delta_p = 4.1 \quad (20)$$

This corresponds to a CR proton luminosity above a particle energy of 10 TeV equal to $W_{CR}(E_p \geq 10 \text{ TeV}) \approx 7 \times 10^{37} \text{ erg s}^{-1}$, which is comparable with the early estimation from the H.E.S.S. Collaboration $\approx 4 \times 10^{37} (D(10 \text{ TeV})/10^{30} \text{ cm}^2 \text{ s}^{-1}) \text{ erg s}^{-1}$ (HESS Collaboration et al. 2016).

The leptonic scenario (right panel of Fig. 4) will be discussed in the next Section.

4. Radio observations of the CMZ

The radio emission from the CMZ region has been mapped by the Very Large Array (VLA) (LaRosa et al. 2005), the Green Bank Telescope (GBT) (Law et al. 2008) and MeerKAT (Heywood et al. 2022). The dominant mechanism for the production of radio waves is the synchrotron radiation from CR electrons.

Hence, the nonthermal radio continuum can be used to probe the intensity of CR electrons close to the GC.

4.1. Derivation of cosmic-ray electron spectrum

Here, we constrain the spectrum of CR electrons in the CMZ from the radio observations of the inner $2^\circ \times 0.85^\circ$ of the GC region taken at 0.325, 1.40, 8.5 and 5 GHz from the GBT (Law et al. 2008; Yusef-Zadeh et al. 2013). To fit this data, we assume that CR electrons are injected at the central source with a spectrum which is a broken power-law in momentum:

$$Q_{p,e}(p) = \begin{cases} Q_* \left(\frac{p}{p_*}\right)^{-\delta_{e,1}}, & \text{if } p \leq p_* \\ Q_* \left(\frac{p}{p_*}\right)^{-\delta_{e,2}}, & \text{otherwise} \end{cases} \quad (21)$$

where $p_*c = 1.5 \text{ GeV}$. Similarly, as in the case for γ -ray emissions, we propagate this injection spectrum using Eq.(8) and the steady-state solution is used to compute synchrotron emissions.

The radio data can be fitted using a broken power-law as defined in Eq.(21) using the following normalisation:

$$Q_{p,e}(10 \text{ TeV}) = 1.5 \times 10^{27} \text{ MeV}^{-1} \text{ s}^{-1} \quad (22)$$

and spectral indices

$$\delta_{e,1} = 3.25 \quad (23)$$

$$\delta_{e,2} = 4.4 \quad (24)$$

where $\delta_{e,1}$ is mostly constrained by radio data, while $\delta_{e,2}$ has been chosen to not overshoot the γ rays. With this respect, the right panel of Fig.(4) shows the observed γ -ray spectrum of the CMZ plotted with the contributions expected from inverse Compton and relativistic Bremsstrahlung produced by the steady-state spectrum obtained from Eq.(21). Note that before computing the synchrotron emission from the ambient (LIS) CRs, we added a low-energy exponential cutoff at an energy of 100 MeV. This is the energy where the CR electron loss time equals the diffusion time across the CMZ (see Fig. 3), and the cutoff is intended to roughly mimic the effect of the penetration of Galactic CRs into the CMZ (see e.g. Dogiel et al. (2021)).

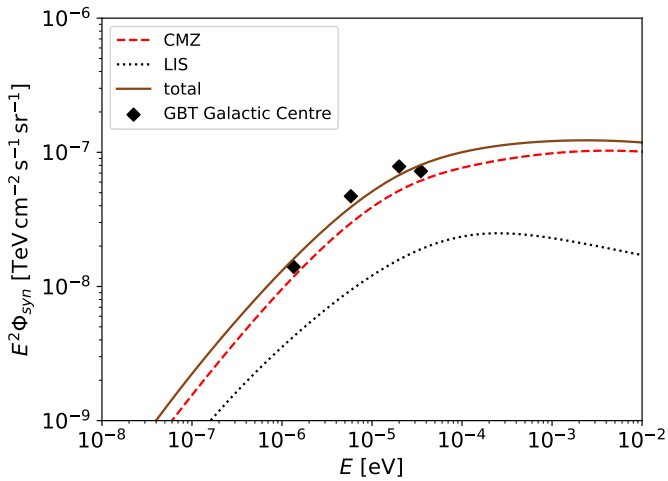


Fig. 5: Fit to radio data from the CMZ region. The solid line refers to the total predicted synchrotron emission from CR electrons. The dashed line shows the contribution from electrons accelerated inside the CMZ. The dotted line shows the contribution from the background sea of CR electrons (LIS) with a low-energy exponential cut-off to take into account the suppressed penetration of background CR electrons into the CMZ. We consider an average magnetic field strength of $B_{CMZ} \sim 150 \mu\text{G}$.

5. Cosmic-ray ionisation rate

Now that we have imposed constraints on the intensity and spectral energy distribution of CR nuclei and electrons in the CMZ, we investigate the impact that these particles have on the gas in the CMZ. In particular, we compute the CR ionisation rate of ambient gas, and we compare that with available measurements of this parameter. To do so, it will be necessary to extrapolate to low energies the CR spectra derived above, as low-energy particles (roughly in the sub-GeV domain) are believed to be the most effective ionisation agents in MCs.

As described in Sec. 1, the ionisation rate of H_2 molecules in dense MCs can be measured by means of observation of molecular lines such as, most notably, those of H_3^+ falling in the IR band (Oka 2006; Miller et al. 2020). This is because the production of H_3^+ in MCs follows in a straightforward way from the ionisation of molecular hydrogen.

If f_p and f_e are the CR particle distribution functions for protons and electrons, respectively, the CR proton and electron ionisation rates can be expressed as:

$$\begin{aligned} \zeta_p &= \int_{E_{min}}^{E_{max}} v_p f_p(E_p) \sigma_p^{ion}(E_p) (1 + \phi_p(E_p)) dE_p \\ &+ \int_0^{E_{max}} v_p f_p(E_p) \sigma_p^{e.c.}(E_p) dE_p \\ \zeta_e &= \int_{E_{min}}^{E_{max}} v_e f_e(E_e) \sigma_e^{ion}(E_e) (1 + \phi_e(E_e)) dE_e \end{aligned} \quad (25)$$

where v_i is the particle velocity, ϕ_i the average number of secondary ionisations per primary ionisation, modelled as in Krause et al. (2015). Available parameterisations of the proton impact ionisation cross section σ_p^{ion} , the electron capture cross section $\sigma_p^{e.c.}$, and the electron impact ionisation cross sections σ_e^{ion} have been reviewed by Padovani et al. (2009) and later improved by Krause et al. (2015) and Gabici (2022). The impact of CR nuclei

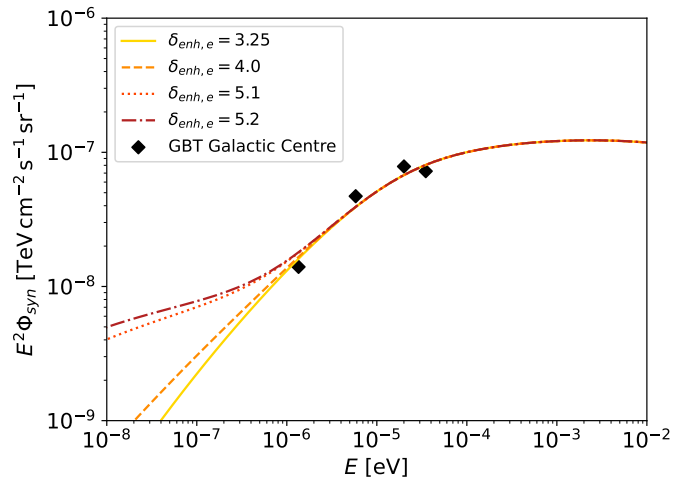


Fig. 6: Expected synchrotron radio emission from the enhanced CR electron injection spectra considered in this work (see main text for details), compared to radio observations of the CMZ.

heavier than protons should also be accounted for when computing the CR ionisation rate. This is done by introducing an enhancement factor $\eta \approx 1.5$ such that the CR ionisation rate of nuclei is $\zeta_n = \eta \zeta_p$ (Padovani et al. 2009). In the following, the term proton ionisation rate will refer to the nuclear-enhanced value.

The electron ionisation cross section peaks in the sub-keV energy range, and any electron of energy larger than the ionisation potential of H_2 , $I = 15.426 \text{ eV}$, will contribute to ionise the ambient gas. Hence, we consider CR electrons of energy larger than $E_{min} = I$.

On the other hand, for ionisation due to CR protons, electron capture dominates over proton impact for particle energies below a few tens of keV (see e.g. Fig. 11 in Gabici 2022). This means that a CR proton cooling below that energy will convert into a fast neutral hydrogen atom and, as a consequence, will become unable to further ionise the gas (e.g. Chabot 2016). For this reason, for protons, we set $E_{min} = 45 \text{ keV}$.

As a first step, the CR proton and electron injection spectra inferred from γ -ray and radio data in the previous section have been extrapolated down to lower energies and propagated using the transport equation solver to obtain steady-state spectra. Then, the CR proton and electron ionisation rates averaged over the entire CMZ volume were computed to find $1.9 \times 10^{-17} \text{ s}^{-1}$ and $3.0 \times 10^{-18} \text{ s}^{-1}$, respectively. These values are much (orders of magnitude) smaller than the measured ones, meaning that an extra component of CRs must be present in order to explain observations.

The extra component (enhancement) is added to the CR injection spectra derived above in the following way:

$$Q_{p,p}(p) = \begin{cases} Q_{enh,p} \left(\frac{p}{p_{enh,p}} \right)^{-\delta_{enh,p}}, & \text{if } p \leq p_{enh,p} \\ Q_{enh,p} \left(\frac{p}{p_{enh,p}} \right)^{-\delta_p}, & \text{otherwise} \end{cases} \quad (26)$$

for protons and

$$Q_{p,e}(p) = \begin{cases} Q_{enh,e} \left(\frac{p}{p_{enh,e}} \right)^{-\delta_{enh,e}}, & \text{if } p \leq p_{enh,e} \\ Q_{enh,e} \left(\frac{p}{p_{enh,e}} \right)^{-\delta_{e,1}}, & \text{if } p_{enh,e} \leq p \leq p_* \\ Q_{enh,e} \left(\frac{p_*}{p_{enh,e}} \right)^{\delta_{e,2}-\delta_{e,1}} \left(\frac{p}{p_{enh,e}} \right)^{-\delta_{e,2}}, & \text{otherwise} \end{cases} \quad (27)$$

for electrons.

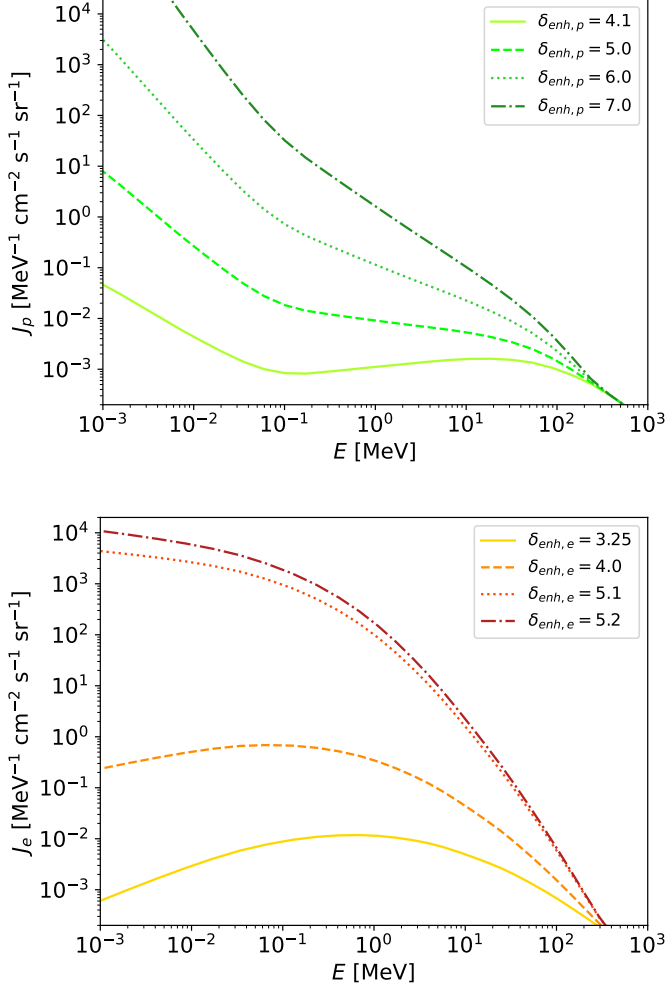


Fig. 7: Steady-state CR intensities for protons (top) and electrons (bottom) averaged over the CMZ volume. Curves refer to different enhancements applied to the CR injection spectrum, as indicated by the parameter $\delta_{enh,i}$.

For particle momenta below $p_{enh,i}$ CR spectra are enhanced with respect to those adopted so far in this paper. For protons we choose $p_{enh,p} \approx 780$ MeV. This momentum corresponds to a kinetic energy $E_p = 280$ MeV, i.e., the threshold for pion production. Adding an enhancement below this momentum will ensure that no γ -rays are produced by the additional component, and therefore, the fits to γ -ray data performed above will be unaffected. For electrons, the transition momentum has been chosen to be equal to $p_{enh,e} \approx 450$ MeV, which ensures that the

fit to radio data obtained above is unaffected. This can be seen in Fig. 6, where the synchrotron radio emission from enhanced electron spectra is shown together with radio data.

The steady-state CR proton and electron intensities averaged over the entire CMZ volume are shown in Fig. 7 for various values of the parameter $\delta_{enh,i}$.

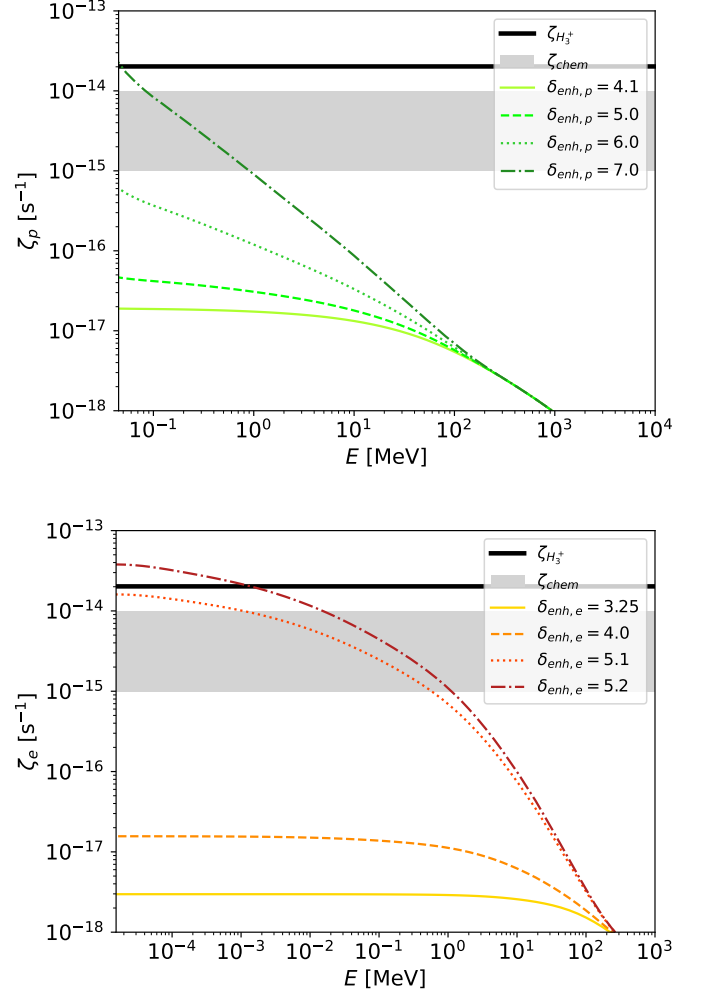


Fig. 8: CR proton (top) and electron (bottom) ionisation rates as a function of the minimum particle energy considered for the CR spectra shown in Fig. 7. Values are averaged over the CMZ volume and compared to the estimated values of ionisation rates derived by different observational methods (horizontal black line and shaded region).

The proton and electron ionisation rates computed using these volume-averaged spectra are shown in Fig. 8 as a function of different minimum ionising particle energy E_{min} (this is the minimum energy appearing in Eq. 25). For comparison, we also plot as a horizontal thick black line the ionisation rate $\zeta_{H_3^+}$ in the GC region obtained from H_3^+ observations, obtained by averaging the measurements from Le Petit et al. (2016); Oka et al. (2019). We also add a grey-shaded region, which gives the range of values for the more conservative ionisation rates ζ_{chem} inferred from measurements of the abundances of other chemical species (Rivilla et al. 2022; Sanz-Novato et al. 2024).

We see from Fig. 8 that in order to reproduce the ionisation rate measurements one needs an extremely steep additional CR

Table 2: Power requirements and energy density for proton spectra as a function of the corresponding proton CR ionisation rate in the CMZ

$\zeta_p(\text{s}^{-1})$	$\delta_{enh,p}$	$E_{min}(\text{MeV})$	$W_{CR}(\text{erg/s})$	$n_{CR}(\text{eV cm}^{-3})$
10^{-15}	7.0	0.9	$3.7 \cdot 10^{39}$	0.48
$2 \cdot 10^{-14}$	7.0	$4.5 \cdot 10^{-2}$	$6.8 \cdot 10^{40}$	0.52

Table 3: Power requirements and energy density for electron spectra as a function of the corresponding electron CR ionisation rate in the CMZ

$\zeta_e(\text{s}^{-1})$	$\delta_{enh,e}$	$E_{min}(\text{MeV})$	$W_{CR}(\text{erg/s})$	$n_{CR}(\text{eV cm}^{-3})$
10^{-15}	5.1	0.6	$2.0 \cdot 10^{39}$	0.36
10^{-15}	5.2	1.1	$2.1 \cdot 10^{39}$	0.45
$2 \cdot 10^{-14}$	5.2	$1.5 \cdot 10^{-3}$	$2.4 \cdot 10^{40}$	0.58

component (slopes larger than $\delta_{enh,p} \sim 7$ and $\delta_{enh,e} \sim 5$ for CR protons and electrons, respectively) extending down to very low particle energies ($E_{min} \approx 1 \text{ keV} - 1 \text{ MeV}$ for both CR protons and electrons). Very steep spectra are needed because the energy loss time of CR particles is very short at sub-GeV energies (see Fig. 3), and therefore, this has to be compensated by the injection of a very large number of low-energy particles (for a discussion of this issue see Recchia et al. 2019). This raises the question - what is the energy budget required to maintain a population of particles capable of reproducing the measured ionisation rate in the CMZ?

To answer this question, we compute two quantities: the power W_{CR} needed to maintain the CR population at a given level in the CMZ and the CR energy density averaged over the entire CMZ volume n_{CR} . These quantities were computed for CR spectra able to reproduce the measurements of the ionisation rates in the CMZ and are reported in Tables 2 and 3 for CR protons and electrons, respectively. Here, we note E_{min} the minimum ionising energy needed for the computed ionisation rate to exceed the measured values.

The powers obtained in this way can be compared with the total CR power of the Milky Way, which can be estimated using the large amount of available CR data. This has been done, among many others, by Strong et al. (2010), who found values in the range $W_{MW}^p \sim 6.0 - 7.4 \times 10^{40} \text{ erg/s}$ and $W_{MW}^e \sim 1.0 - 1.7 \times 10^{39} \text{ erg/s}$ for CR protons and electrons, respectively. The comparisons with these figures show that the powers reported in Tables 2 and 3 are extremely large.

In order to reproduce the values of the ionisation rate measured in the CMZ, CR electrons should be injected by the source located in the GC at a rate that is larger than the total injection rate of CR electrons in the entire Milky Way! For CR protons, the required power has to be comparable to the total CR proton power of the Milky Way in order to reproduce an ionisation rate of the order of 10^{-14} s^{-1} , and about half of it to reproduce an ionisation rate of the order of 10^{-15} s^{-1} . Moreover, this huge amount of energy should have as unique manifestation the enhancement in the gas ionisation rate in the CMZ region.

One can also compare the CR powers obtained above with characteristic powers connected to the supermassive black hole at the centre of the Milky Way. It has been estimated that the mechanical power needed to inflate the giant ($\gtrsim 10 \text{ kpc}$) bubbles discovered by Fermi (Su et al. 2010) and eROSITA (Predehl et al. 2020) is of the order of $P_b \approx 10^{41} \text{ erg/s}$, and that the injection of energy should last few tens of million years (Sarkar

2024). This is of the same order of the energy required to maintain a population of CR protons capable of ionising the CMZ gas at a rate of $\approx 10^{-14} \text{ s}^{-1}$ and about four times the energy needed in CR electrons to reach the same rate (see last row of both Table 2 and 3). It follows that it is quite challenging to explain the large ionisation rates with CRs, while lower values ($\approx 10^{-15} \text{ s}^{-1}$) might still be acceptable.

However, another observable that should be reproduced is the fact that roughly the same ionisation rate has been obtained by analysing H_3^+ lines from several lines of sights across the CMZ (at least up to 100 pc radius, Indriolo et al. 2015). The ionisation rate measured in this way does not show any clear spatial variation and is indeed compatible with a constant value across the CMZ. This trend cannot be reproduced by our model, as shown Fig. 10. There, the CR ionisation rate averaged along the lines of sights laying along the Galactic plane at different distances R from the GC. The predicted trend for CR protons (top) and electrons (bottom panel) clearly does not explain observations.

We note here that the mass of the CMZ that has been chosen to derive the values reported in Tables 2 and 3, though widely used in the literature, is the maximum amongst the various measurements found in the literature (which is $2 - 6 \times 10^7 M_\odot$, as reported in Dahmen et al. 1998). We repeated our entire study for the lower limit of $M_{CMZ} = 2 \times 10^7 M_\odot$ and found that the power needed to sustain ionisation rates at $\approx 10^{-14} \text{ s}^{-1}$ are also in this case of the order of $\gtrsim 10^{40} \text{ erg s}^{-1}$ for protons and $\gtrsim 10^{39} \text{ erg s}^{-1}$ for electrons. This is because a lower mass (and therefore gas density) would require a larger density of high energy CRs to explain the γ ray and radio emissions, but at the same time, would reduce the effects of ionisation losses. The two effects then compensate.

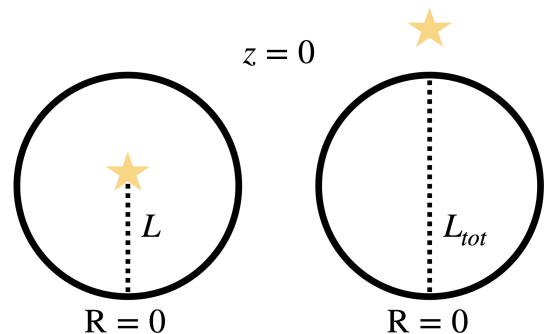


Fig. 9: Position of the star used to measure the column density of H_3^+ with respect to the CMZ. L is the distance from the front of the CMZ to the position of the star. $L_{tot} = 2R_{CMZ}$ is the longest distance through the CMZ in any line of sight.

Before concluding, we should notice that the measurements of H_3^+ column densities rely on the presence of a background star. However, the distance to these stars is a major source of uncertainty in the measurements. In fact, the results we presented so far assumed implicitly that the stars are located behind the CMZ (as illustrated in the right panel of Fig. 9). If, instead, the star is located within the CMZ (as in the left panel of Fig. 9), the average of the predicted CR ionisation rate should be performed over the length L .

Fig. 11 shows the CR ionisation rates averaged from the edge of the CMZ to a depth L , for lines of sight passing through the point $z = 0$ and $R = 0$. In such a plot, the ionisation rate averaged over the entire line of sight is represented by the rightmost

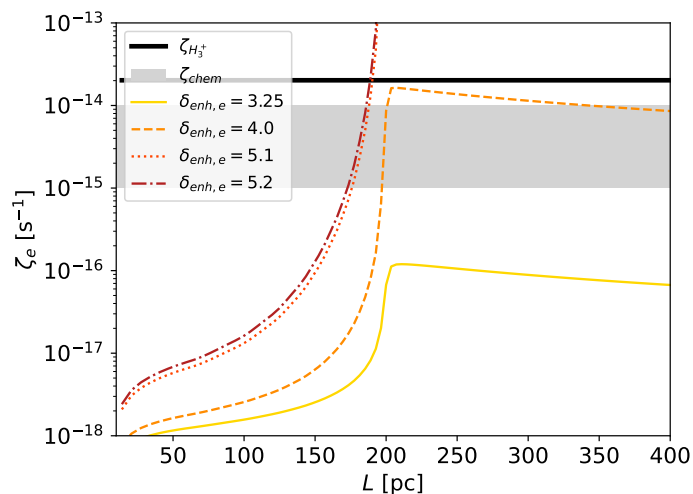
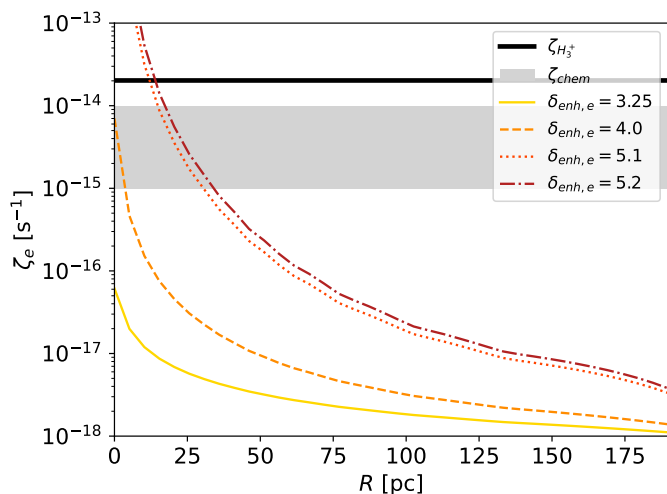
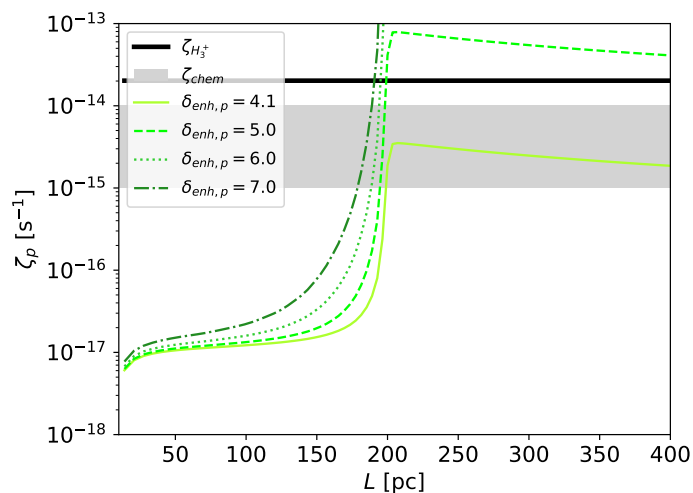
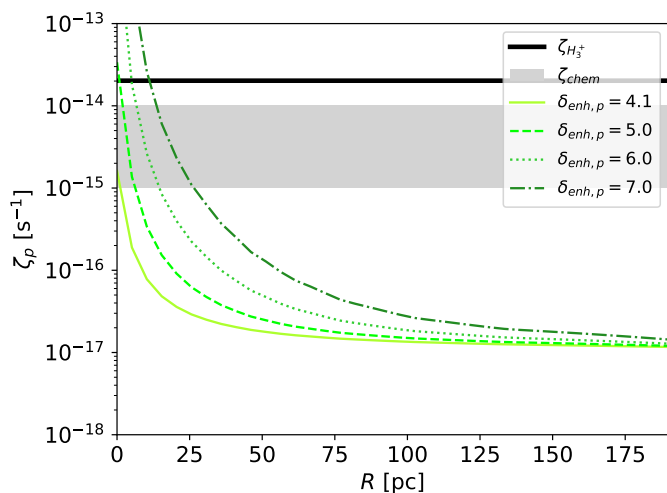


Fig. 10: CR proton (top) and electron (bottom) ionisation rates averaged over lines of sight at different projected distances R from the GC. The horizontal lines and shaded regions and the values of $\delta_{enh,i}$ are as in Fig. 8.

value of the curves. The figure shows that if the star is located closer to us than the GC, then one would expect to measure much lower ionisation rates, while only a very slight enhancement of the average ionisation rate is expected for locations $L \gtrsim R_{CMZ}$. This makes it even more difficult (if not impossible) to explain the large ionisation rates derived from observations. Notice also that the plot refers to a line of sight passing through the centre of the CMZ ($R = 0$ and $z = 0$) and, therefore, corresponds to the maximum possible values of the ionisation rate (as illustrated by Fig. 10).

6. Additional constraints on MeV particles

6.1. MeV γ -rays

CRs in the MeV and sub-MeV domains contribute the most to the ionisation rate. Electrons of this energy also emit non-thermal Bremsstrahlung photons in the hard-X/soft- γ -ray bands. The emission from the Galactic disk in this energy domain has been observed by the SPectrometer on INTEGRAL (SPI) and by the imaging Compton telescope COMPTEL. We use data points

Fig. 11: CR proton (top) and electron (bottom) ionisation rates averaged over different lengths of lines of sight. The horizontal lines and shaded regions and the values of $\delta_{enh,i}$ are as in Fig. 8.

from Bouchet et al. (2011), but more recent data (Siegert et al. 2022) are consistent with these earlier findings. γ -ray spectra have been extracted for the inner Galaxy region defined by the coordinate ranges $|l| < 30^\circ$ and $|b| < 15^\circ$. As this region is much larger than that considered in this paper, these values should be considered as an upper limit for the γ -ray flux of the CMZ.

In Fig. 12, we show this data along with the predicted γ -ray emissions in this energy range from CR electrons with a spectrum corresponding to an ionisation rate equal to 10^{-15} and $2 \times 10^{-14} \text{ s}^{-1}$ (see Figure inset and Table 3). The MeV γ -ray flux is largely dominated by Bremsstrahlung radiation, and the inverse Compton scattering contribution is largely subdominant. Remarkably, the predicted γ -ray flux exceeds observed data, and this rules out scenarios where low-energy CR electrons are responsible for the high ionisation rates measured in the CMZ.

6.2. Iron $K\alpha$ line

The X-ray emission line at 6.4 keV results from the ionisation of iron atoms by the ejection of a K-shell electron. The diffuse X-ray emission from the CMZ has a variable and a constant component. The variable component is believed to be the reflection by

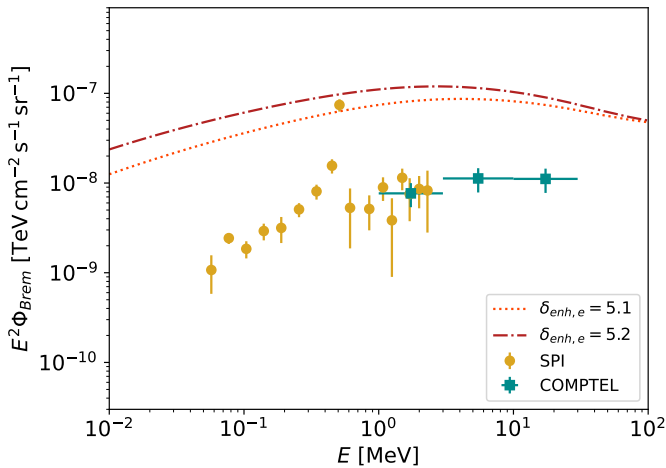


Fig. 12: Bremsstrahlung γ -rays from electron spectra capable of giving ionisation rate above 10^{-15} s^{-1} compared to SPI and COMPTEL data from the inner galaxy $|l| < 30^\circ$ and $|b| < 15^\circ$ from Bouchet et al. (2011).

the MCs of a past X-ray outburst from the SMBH, which is why it is decreasing over time (Terrier et al. 2018). A constant component is expected from the supposed constant density of CRs ionising the region (Capelli et al. 2012). Since the observations of the CMZ over several years show a decreasing flux, the most recent measurement of the Fe $K\alpha$ line flux is only an upper limit for the contribution from the CRs. The most recent observation of the inner 300 pc was conducted by XMM-Newton in 2012. Other more recent surveys of specific regions exist (Kuznetsova et al. 2022). This survey has revealed that the 6.4 keV line flux in 2012 was $1.507 \pm 0.009 \times 10^{-3} \text{ ph cm}^{-2} \text{ s}^{-1}$ from a $19 \times 112 \text{ arcmin}^2$ area (Terrier et al. 2018). The corresponding average surface brightness is $7.36 \pm 0.04 \times 10^{-7} \text{ ph cm}^{-2} \text{ s}^{-1} \text{ arcmin}^{-1}$.

The intensity of the Fe $K\alpha$ line resulting from CR interactions can be expressed as:

$$I_i^{K\alpha} = \frac{M_{CMZ}}{4\pi D_{GC}^2 m_{avg}} \int_{E_{min}}^{E_{max}} \eta_{Fe} \sigma_i^{K\alpha}(E_i) v_i f_i(E_i) dE_i \quad (28)$$

where i represents the species of the CR particle, $\sigma_i^{K\alpha}$ is the K-shell ionisation cross-section by CR species i (Tatischeff et al. 2012) considering solar abundance of iron ($\eta_{Fe} = 3 \times 10^{-5}$) and $m_{avg} = 1.4 m_H$ the average particle mass.

We compute the Fe $K\alpha$ average surface brightness from the CMZ using the proton and electron spectra that give ionisation rates above 10^{-15} s^{-1} . The values are given in Tables 4 and 5. The iron abundance in the CMZ is expected to be higher than that of the solar neighbourhood. Hence, the values of the Fe $K\alpha$ line emissions are a lower limit for what is expected from the CR spectra.

Table 4: Fe $K\alpha$ average surface brightness from CR protons

$\zeta_p(\text{s}^{-1})$	$\delta_{enh,p}$	$E_{min}(\text{MeV})$	$B_p^{K\alpha}(\text{ph cm}^{-2} \text{ s}^{-1} \text{ arcmin}^{-2})$
10^{-15}	7.0	0.9	5.8×10^{-10}
2×10^{-14}	7.0	4.5×10^{-2}	5.8×10^{-10}

The expected Fe $K\alpha$ surface brightness over the CMZ resulting from CR ionisation is lower by a few orders of magnitude than the observed rate. This estimate may increase if the correct

Table 5: Fe $K\alpha$ average surface brightness from CR electrons

$\zeta_e(\text{s}^{-1})$	$\delta_{enh,e}$	$E_{min}(\text{MeV})$	$B_e^{K\alpha}(\text{ph cm}^{-2} \text{ s}^{-1} \text{ arcmin}^{-2})$
10^{-15}	5.1	0.6	7.8×10^{-9}
10^{-15}	5.2	1.1	8.3×10^{-9}
2×10^{-14}	5.2	1.5×10^{-3}	5.1×10^{-8}

iron abundance is used instead of solar abundance, but the enhancement would be, at most, a factor of a few and, therefore, not sufficient to enhance our prediction of the observed values. Hence, Fe $K\alpha$ line observations can not help constrain the spectrum of low-energy CRs in the CMZ. Indeed, this agrees with what was claimed by Dogiel et al. (2013), where it was argued that the contribution to the 6.4 keV line from low-energy CRs responsible for the high ionisation rates must be negligible.

7. Discussion and conclusion

The main conclusion of this paper is that it is extremely unlikely that CRs in the CMZ are the agents responsible for the large ionisation rates derived from a number of observations.

Motivated by the results coming from γ -ray observations of the CMZ, we investigated a scenario where a powerful accelerator of CR is located in the centre of the Galaxy. The accelerator is assumed to continuously inject CRs in the surrounding medium. Once injected, CRs diffuse away from the GC and fill the CMZ.

Fitting the γ -ray and radio emission from the CMZ allowed us to constrain the high-energy spectra of CR particles there. We found that a simple power-law extrapolation of such spectra at low energies fails by orders of magnitude to reproduce the measured values of the ionisation rate of molecular hydrogen.

We then added an additional, steep, low-energy CR component in an attempt to explain the large values of the ionisation rate without violating any other observational constraint. We showed that the injection power of energetic particles required to explain ionisation rates at the level of $\approx 10^{-14} \text{ s}^{-1}$ is exceedingly large: $\sim 7 \times 10^{40} \text{ erg s}^{-1}$ for protons and $\sim 2 \times 10^{40} \text{ erg s}^{-1}$ for electrons. This is comparable to the total power P_b required to inflate the giant eROSITA bubbles. More conservative estimates of the ionisation rate ($\approx 10^{-15} \text{ s}^{-1}$) could be explained if a few per cent of the power P_b could be somehow converted into CRs.

In fact, this unrealistic large power estimation for low-energy CRs is obtained when using the most conservative values for the transport parameters. We choose the diffusion coefficient, the Galactic wind velocity, and the Alfvén speed to maximise the duration for which cosmic rays stay within the CMZ. Hence, we argue that using different values for all these parameters would further increase the power required.

However, the CR energy budget is not the only issue. CRs escaping from an accelerator located at the GC would generate an ionisation rate that declines quite steeply as the distance from the GC increases. This is not observed in data that show a roughly constant value of the ionisation rate throughout the CMZ. Uncertainties in the exact location of the stars used to make it even more difficult to fit out model results to data. In fact, these high ionisation rates are also expected in the cores of dense MCs where Yang et al. (2023) showed that CRs below $\lesssim \text{GeV}$ are prevented from entering such MCs.

We note that the CR energy densities found in our model (see last column of Tables 2 and 3) are quite modest. This was also pointed out in a previous study by Dogiel et al. (2015). However, we have stressed here that the power needed to maintain these

modest energy densities of CRs is extremely large, mainly due to the very short energy loss time of sub-relativistic particles (see Fig. 2 and times), and that this makes a CR origin of the large ionisation rates very unlikely.

A different scenario could be envisaged where an impulsive rather than continuous source of CRs is present. In that case, however, the large ionisation rates would be a transient phenomenon, and this would add an additional parameter (i.e. the time since the impulsive injection) to be fine-tuned. An inspection of Fig. 3 can help in characterising what could be the optimal setup for this scenario. The duration of the enhanced ionisation rates would be of the order of $\Delta t \lesssim 10^5$ yr, which is the characteristic diffusion time of ≈ 100 MeV CRs across the CMZ. Such particles would lose their energy in a time comparable to the diffusion time across the CMZ. A naive but probably not too inaccurate estimate of the total required energy in this scenario is given by the product $\mathcal{E}_{tot} \approx W_{CR} \times \Delta t$, where for W_{CR} one can adopt the values reported in Table 3 and 2. This would give $\mathcal{E}_{tot} \approx 3 \times 10^{52} (W_{CR}/10^{40} \text{ erg/s})(\Delta t/10^5 \text{ yr})$ erg. Remarkably, this is of the same order of the thermal energy of the X-ray chimneys ($\sim 4 \times 10^{52}$ erg), which are characterised by a sound crossing time equal to $\sim 3 \times 10^5$ yr, which is comparable to Δt (Ponti et al. 2019). The chimneys are the exhaust channels through which mass and energy ejected from the supermassive black hole in the GC are channelled out of the Galactic disk. The similarity between their total energy and that needed in low-energy CRs suggests that also a scenario based on an impulsive injector of particles would face severe problems based on global energetic constraints.

Finally, the rough spatial uniformity of the values of the ionisation rate could be explained if many CR sources distributed across the entire CMZ inject energetic particles. In this case, the energetic problem could be even more severe, as the source of energy would not be connected to the supermassive black hole located at the GC. As an example, the rate at which mechanical energy is injected in the CMZ due to supernova explosions is $\approx 10^{40}$ erg/s (see Jouvin et al. 2017, and references therein), which is one order of magnitude smaller than P_b .

We conclude that a source of ionisation of molecular hydrogen in the CMZ other than CRs is very likely to exist. The most obvious candidate is a radiation field made of UV and/or X-ray photons. As it is known that X-ray photons emitted by Sgr A* during outbursts do not suffice to explain the observed ionisation rates (Dogiel et al. 2013), the sources of ionising photons will have to be distributed across the entire CMZ. Further studies in this direction are therefore needed.

Acknowledgements. The authors acknowledge helpful advice on the code from Sebastian-Achim Müller, Francesco Conte, Ludwig M. Böss, Enrico Peretti and Alexandre Inventar. We are also thankful for the inspiring discussions on low-energy CRs in the GC region with Andrea Goldwurm, Marianne Lemoine-Goumard, Denis Allard, Rui-zhi Yang, Richard Tuffs, Jim Hinton, Bing Liu, Adam Ginsburg and Thushara Pillai. This study was supported by the LabEx UnivEarthS, ANR-10-LABX-0023 and ANR-18-IDEX-0001. V.H.M.P. acknowledges support from the Initiative Physique des Infinis (IPI), a research training program of the IDEX SUPER at Sorbonne Université. S.G. acknowledges support from Agence Nationale de la Recherche (grant ANR-21-CE31-0028).

References

Adams, C. B., Benbow, W., Brill, A., et al. 2021, *ApJ*, 913, 115
 Aharonian, F., Akhperjanian, A. G., Bazer-Bachi, A. R., et al. 2006, *Nature*, 439, 695
 Bouchet, L., Strong, A. W., Porter, T. A., et al. 2011, *ApJ*, 739, 29
 Capelli, R., Warwick, R. S., Porquet, D., Gillessen, S., & Predehl, P. 2012, *A&A*, 545, A35
 Caselli, P., Walmsley, C. M., Terzieva, R., & Herbst, E. 1998, *ApJ*, 499, 234

Chabot, M. 2016, *A&A*, 585, A15
 Crocker, R. M., Jones, D. I., Aharonian, F., et al. 2011, *MNRAS*, 413, 763
 Crocker, R. M., Jones, D. I., Melia, F., Ott, J., & Protheroe, R. J. 2010, *Nature*, 463, 65
 Dahmen, G., Huttemeister, S., Wilson, T. L., & Mauersberger, R. 1998, *A&A*, 331, 959
 Dogiel, V. A., Chernyshov, D. O., Ivlev, A. V., Kiselev, A. M., & Kopyev, A. V. 2021, *ApJ*, 921, 43
 Dogiel, V. A., Chernyshov, D. O., Kiselev, A. M., et al. 2015, *ApJ*, 809, 48
 Dogiel, V. A., Chernyshov, D. O., Tatischeff, V., Cheng, K. S., & Terrier, R. 2013, *ApJ*, 771, L43
 Evoli, C., Gaggero, D., Vittino, A., et al. 2017, *J. Cosmology Astropart. Phys.*, 2017, 015
 Ferrière, K., Gillard, W., & Jean, P. 2007, *A&A*, 467, 611
 Gabici, S. 2022, *A&A Rev.*, 30, 4
 Gaggero, D., Grasso, D., Marinelli, A., Taoso, M., & Urbano, A. 2017, *Phys. Rev. Lett.*, 119, 031101
 Geballe, T. R. & Oka, T. 2010, *ApJ*, 709, L70
 Ginsburg, A., Henkel, C., Ao, Y., et al. 2016, *A&A*, 586, A50
 Goto, M., Geballe, T. R., Indriolo, N., et al. 2014, *ApJ*, 786, 96
 Goto, M., Usuda, T., Geballe, T. R., et al. 2011, *PASJ*, 63, L13
 Henshaw, J. D., Barnes, A. T., Battersby, C., et al. 2023, in *Astronomical Society of the Pacific Conference Series*, Vol. 534, *Protostars and Planets VII*, ed. S. Inutsuka, Y. Aikawa, T. Muto, K. Tomida, & M. Tamura, 83
 HESS Collaboration, Abramowski, A., Aharonian, F., et al. 2016, *Nature*, 531, 476
 Heywood, I., Rammala, I., Camilo, F., et al. 2022, *ApJ*, 925, 165
 Hinton, J. A. & Aharonian, F. A. 2007, *ApJ*, 657, 302
 Indriolo, N. & McCall, B. J. 2012, *ApJ*, 745, 91
 Indriolo, N., Neufeld, D. A., Gerin, M., et al. 2015, *ApJ*, 800, 40
 Jouvin, L., Lemièrre, A., & Terrier, R. 2017, *MNRAS*, 467, 4622
 Kafexhiu, E., Aharonian, F., Taylor, A. M., & Vila, G. S. 2014, *Phys. Rev. D*, 90, 123014
 Khangulyan, D., Aharonian, F. A., & Kelner, S. R. 2014, *ApJ*, 783, 100
 Kissmann, R. 2014, *Astroparticle Physics*, 55, 37
 Krause, J., Morlino, G., & Gabici, S. 2015, in *International Cosmic Ray Conference*, Vol. 34, 34th International Cosmic Ray Conference (ICRC2015), 518
 Kuznetsova, E., Krivoson, R., Lutovinov, A., & Clavel, M. 2022, *MNRAS*, 509, 1605
 LaRosa, T. N., Brogan, C. L., Shore, S. N., et al. 2005, *ApJ*, 626, L23
 Law, C. J., Yusef-Zadeh, F., Cotton, W. D., & Maddalena, R. J. 2008, *ApJS*, 177, 255
 Le Petit, F., Nehmé, C., Le Bourlot, J., & Roueff, E. 2006, *ApJS*, 164, 506
 Le Petit, F., Ruaud, M., Bron, E., et al. 2016, *A&A*, 585, A105
 MAGIC Collaboration, Acciari, V. A., Ansoldi, S., et al. 2020, *A&A*, 642, A190
 McCall, B. J., Huneycutt, A. J., Saykally, R. J., et al. 2003, *Nature*, 422, 500
 McKee, C. F. 1989, *ApJ*, 345, 782
 Miller, S., Tennyson, J., Geballe, T. R., & Stallard, T. 2020, *Reviews of Modern Physics*, 92, 035003
 Neufeld, D. A. & Wolfire, M. G. 2017, *ApJ*, 845, 163
 Oka, T. 2006, *Proceedings of the National Academy of Science*, 103, 12235
 Oka, T., Geballe, T. R., Goto, M., et al. 2019, *ApJ*, 883, 54
 Oka, T., Geballe, T. R., Goto, M., Usuda, T., & McCall, B. J. 2005, *ApJ*, 632, 882
 Padovani, M., Galli, D., & Glassgold, A. E. 2009, *A&A*, 501, 619
 Padovani, M., Ivlev, A. V., Galli, D., & Caselli, P. 2018, *A&A*, 614, A111
 Phan, V. H. M., Morlino, G., & Gabici, S. 2018, *MNRAS*, 480, 5167
 Phan, V. H. M., Recchia, S., Mertsch, P., & Gabici, S. 2023, *Phys. Rev. D*, 107, 123006
 Phan, V. H. M., Schulze, F., Mertsch, P., Recchia, S., & Gabici, S. 2021, *Phys. Rev. Lett.*, 127, 141101
 Ponti, G., Hofmann, F., Churazov, E., et al. 2019, *Nature*, 567, 347
 Predehl, P., Sunyaev, R. A., Becker, W., et al. 2020, *Nature*, 588, 227
 Press, W. H., Teukolsky, S. A., Vetterling, W. T., & Flannery, B. P. 1992, *Numerical Recipes in C*, 2nd edn. (Cambridge, USA: Cambridge University Press)
 Recchia, S., Phan, V. H. M., Biswas, S., & Gabici, S. 2019, *MNRAS*, 485, 2276
 Rivilla, V. M., García De La Concepción, J., Jiménez-Serra, I., et al. 2022, *Frontiers in Astronomy and Space Sciences*, 9, 829288
 Sanz-Novato, M., Rivilla, V. M., Jiménez-Serra, I., et al. 2024, *ApJ*, 965, 149
 Sarkar, K. C. 2024, *A&A Rev.*, 32, 1
 Schlickeiser, R. 2002, *Cosmic Ray Astrophysics*
 Siebert, T., Berteaud, J., Calore, F., Serpico, P. D., & Weinberger, C. 2022, *A&A*, 660, A130
 Strong, A. W., Porter, T. A., Digel, S. W., et al. 2010, *ApJ*, 722, L58
 Su, M., Slatyer, T. R., & Finkbeiner, D. P. 2010, *ApJ*, 724, 1044
 Tatischeff, V., Decourchelle, A., & Maurin, G. 2012, *A&A*, 546, A88
 Terrier, R., Clavel, M., Soldi, S., et al. 2018, *A&A*, 612, A102
 Thornbury, A. & Drury, L. O. 2014, *MNRAS*, 442, 3010
 Tsuboi, M., Handa, T., & Ukita, N. 1999, *ApJS*, 120, 1
 van der Tak, F. F. S., Belloche, A., Schilke, P., et al. 2006, *A&A*, 454, L99
 Wolfire, M. G., McKee, C. F., Hollenbach, D., & Tielens, A. G. G. M. 2003, *ApJ*, 587, 278
 Yang, R.-z., Li, G.-X., Wilhelmi, E. d. O., et al. 2023, *Nature Astronomy*, 7, 351
 Yusef-Zadeh, F., Hewitt, J. W., Wardle, M., et al. 2013, *ApJ*, 762, 33
 Yusef-Zadeh, F., Munro, M., Wardle, M., & Lis, D. C. 2007, *ApJ*, 656, 847